Correspondence to:

X. Yu,
yuxlong5@mail.sysu.edu.cn

Observed Equatorward Propagation and Chimney Effect of Near-Inertial Waves in the Midlatitude Ocean

Xiaolong Yu[1,2,3] [ID], **Alberto C. Naveira Garabato[4]** [ID], **Clément Vic[5]** [ID], **Jonathan Gula[5,6]** [ID], **Anna C. Savage[7], Jinbo Wang[8], Amy F. Waterhouse[7]** [ID], **and Jennifer A. MacKinnon[7]** [ID]

[1]School of Marine Sciences, Sun Yat-sen University, Zhuhai, China, [2]Southern Marine Science and Engineering Guangdong Laboratory, Zhuhai, China, [3]Guangdong Provincial Key Laboratory of Marine Resources and Coastal Engineering, Guangzhou, China, [4]Ocean and Earth Science, University of Southampton, Southampton, UK, [5]Laboratoire d'Océanographie Physique et Spatiale (LOPS), University Brest, CNRS, IRD, Ifremer, IUEM, Brest, France, [6]Institut Universitaire de France (IUF), Paris, France, [7]Scripps Institution of Oceanography, University of California, San Diego, CA, USA, [8]M/S 300-323C, 4800 Oak Grove Drive, Pasadena, CA, USA

Abstract The propagation characteristics of near-inertial waves (NIWs) and how mesoscale and submesoscale processes affect the waves' vertical penetration are investigated using observations from a mooring array located in the northeast Atlantic. The year-long observations show that near-inertial motions are mainly generated by local wind forcing, and that they radiate equatorward and downward following several strong wind events (wind stress $\gtrsim 0.5$ N m^{-2}). Observational estimates of horizontal group speed typically exceed those of vertical group speed by two orders of magnitude, consistent with predictions from the dispersion relation. Enhanced near-inertial kinetic energy and vertical shear are found only in mesoscale anticyclones with Rossby number of O(0.1). By contrast, submesoscale motions with order one Rossby number have little effect on the trapping and vertical penetration of NIWs, due to their smaller horizontal scales, shorter time scales, and confined vertical extent compared to mesoscale eddies.

Plain Language Summary Near-inertial waves (NIWs) are excited mainly by variable winds at the ocean surface and can carry their energy into the ocean interior, thus playing an important role in mixing the deep ocean. However, the propagation behaviors of NIWs, and how such waves are affected by mesoscale and submesoscale processes, are still understudied, especially over periods of months to years. In this study, we examine an annual cycle of wind-generated NIWs based on moored observations in a typical open-ocean region of the northeast Atlantic. Our results show that NIWs propagate downward and equatorward following several strong wind events. Enhanced near-inertial kinetic energy and vertical shear are found preferentially in regions of anticyclonic vorticity with Rossby number of O(0.1). By contrast, submesoscale anticyclones with Rossby number of O(1) are ineffective at trapping and accelerating near-inertial motions into the ocean interior. This is due to the smaller horizontal scales, shorter time scales, and confined vertical extent of submesoscale motions compared to mesoscale eddies. Our findings highlight the major role of mesoscale anticyclones in draining NIWs from the upper ocean to the ocean interior, and have implications for detecting regions of active turbulent mixing driven by NIWs in the deep ocean.

1. Introduction

Near-inertial waves (NIWs), primarily generated by strong resonant winds blowing on the sea surface, are crucial contributors to ocean mixing (Alford et al., 2016; Thomas & Zhai, 2022). NIWs are oscillatory, unbalanced internal wave motions with frequencies close to the local inertial frequency, and account for a major portion of internal wave energy and shear (Garrett, 2001). Wind generation of near-inertial motions can be generally considered as a two-stage process, featuring an initial stage with resonant wind work on the ocean surface currents that generates surface mixed-layer near-inertial oscillations, and a subsequent stage with propagation and decay of those motions in the form of NIWs. Global estimates of the wind energy flux into NIWs are in the range of 0.3–1.5 TW (Jiang et al., 2005; Rimac et al., 2013), which is comparable to the global energy conversion rate from external to internal tides in the deep ocean (about 1 TW; Egbert & Ray, 2000). Aside of 15%–25% of the energy input by the wind work radiating away from their generation regions in the form of low-mode NIWs (Alford, 2003; Alford & Zhao, 2007; Simmons & Alford, 2012), over half of the near-inertial energy is thought to locally dissipate in the upper few hundred meters of the ocean (Alford, 2020; Zhai et al., 2009). Nevertheless, the rest of the wave

energy has been suggested to radiate downward (e.g., Gill, 1984; Leaman & Sanford, 1975) and to penetrate to large depths (e.g., 3,000 m; Silverthorne & Toole, 2009). Hence, the substantial downward-propagating NIWs are an important source of energy for driving deep-ocean mixing and maintaining abyssal stratification (Ferrari & Wunsch, 2009; Qu et al., 2021; Whalen et al., 2020).

A key factor that affects the vertical penetration of NIWs is the background vorticity. The principal effect of vorticity is to shift the lower bound of the internal wave band from the local inertial frequency f to the effective inertial frequency, $f_{eff} = f + \zeta/2$, where ζ is the vertical component of the relative vorticity (Kunze, 1985). Consequently, NIWs can be trapped in regions of anticyclonic vorticity where f_{eff} is lower than f. Lee and Niiler (1998) first termed "the inertial chimney effect" the trapping and accumulation of near-inertial energy in regions of anticyclonic vorticity. This effect has been explored by, for example, Zhai et al. (2005); Zhai et al. (2007), who analyzed mesoscale-permitting numerical simulations to show that anticyclonic eddies act to drain the near-inertial energy from the surface to the deep ocean. More recently, the inertial chimney effect of turbulent baroclinic quasi-geostrophic eddies was also demonstrated by Asselin and Young (2020) under an idealized storm scenario, where they referred to this effect as "inertial drainpipe." Vic et al. (2021) examined the association of mooring-measured near-inertial energy with altimetry-derived relative vorticity with a horizontal resolution of O(100 km) over the Mid-Atlantic Ridge, and showed that near-inertial energy is preferentially funneled down within anticyclonic flows. To our knowledge, observational assessment of the chimney effect down to the submesoscales (0.1–10 km) has not yet been performed.

Compared to the vertical propagation of NIWs, their meridional propagation, however, remains elusive. The theory of β-refraction predicts an equatorward propagation of NIWs due to latitudinal variation in the inertial frequency (Garrett, 2001). This proposition is endorsed by near-inertial energy flux estimates from mooring observations in the open ocean (e.g., Alford, 2003) and on the continental shelf (e.g., Schlosser et al., 2019). Such calculations typically require a flat-bottomed ocean and full-depth measurements, and thus existing observations are sparse. By contrast, numerical and observational studies have also shown that NIWs can propagate poleward. Based on turning-point theory and a numerical model, Fu (1981) suggested that the observed local inertial peak over smooth topography could be interpreted in terms of poleward-propagating waves generated at lower latitudes. The poleward propagation of NIWs can also be caused by the background flow (e.g., Huang et al., 2021; Jeon et al., 2019; Tort & Winters, 2018). Tort and Winters (2018) demonstrated a scale selection mechanism by which the super-inertial component of NIWs is able to propagate poleward over long distances in the presence of mesoscale turbulence with horizontal scales considerably smaller than the width of the storm track.

In this study, we focus on the propagation of NIWs in a typical mid-ocean region using nine year-long mooring records that resolve the spatio-temporal scales of the submesoscales. We show that wind-generated NIWs propagate equatorward and downward in the study region. The waves' vertical and meridional group speeds are directly quantified from observations, and are found to be consistent with the properties determined by the dispersion relation. The inertial chimney effect is observed below the mixed layer. However, enhanced near-inertial kinetic energy and vertical shear are only found in mesoscale anticyclones of Rossby number O(0.1) rather than in submesoscale anticyclones of Rossby number O(1).

2. Observations and Methods

2.1. Mooring Observations

Nine bottom-anchored subsurface moorings were deployed over the Porcupine Abyssal Plain (48.63–48.75°N, 16.09–16.27°W) site in the northeast Atlantic Ocean for the period September 2012 - September 2013 (Figure 1a), as part of the Ocean Surface Mixing, Ocean Submesoscale Interaction Study (OSMOSIS) experiment (Buckingham et al., 2016, 2019; Naveira Garabato et al., 2022; Yu et al., 2019, 2021). The mooring site is over a smooth abyssal plain of depth close to 4,800 m. This region is expected to be representative of the midlatitude open ocean far away from western boundaries and complex topography. The nine moorings were arranged in two concentric quadrilaterals with side lengths of ~13 km (outer cluster) and ~2 km (inner cluster) around a centrally located single mooring (Figure 1b). Mooring sensors comprised a series of paired Nortek Aquadopp acoustic current meters (ACMs) and Seabird MicroCAT conductivity-temperature-depth (CTD) sensors at different depths, spanning the approximate depth interval by 30–530 m. The central mooring was the most heavily instrumented, with 13 CTD/ACM pairs. The inner and outer moorings had seven and five such pairs, respectively.
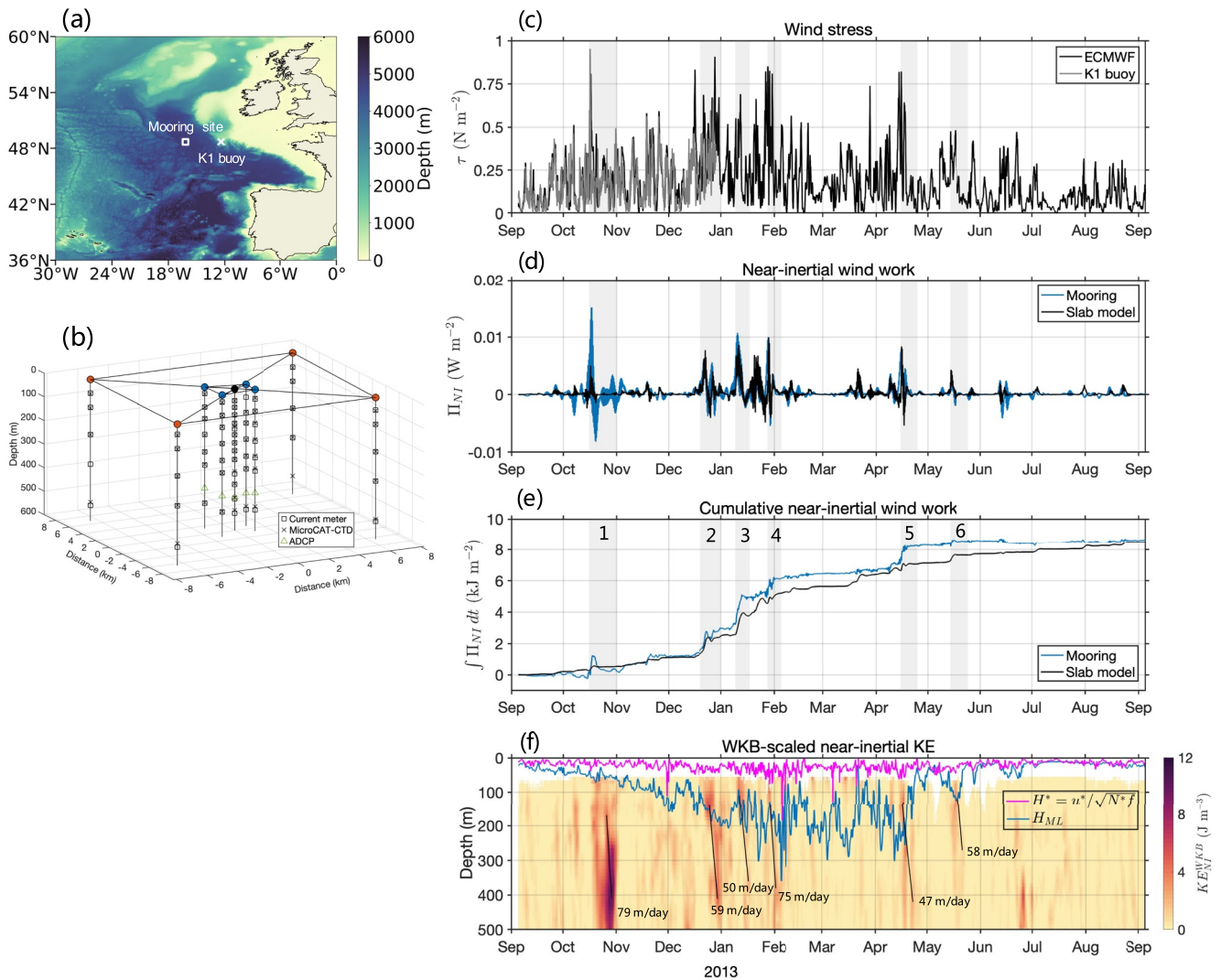
Figure 1. (a) Ocean Surface Mixing, Ocean Submesoscale Interaction Study (OSMOSIS) study region in the Northeast Atlantic, with bathymetry shown in the colormap on the right. The white rectangle and white cross denote the locations of the OSMOSIS mooring array and the K1 buoy, respectively. (b) 3-d configuration of the OSMOSIS array (central mooring marked by black circle, inner moorings by blue circles, and outer moorings by red circles), with positions of current meters, conductivity-temperature-depths (CTDs), and Acoustic Doppler Current Profilers (ADCPs) respectively marked by black squares, black crosses, and green triangles. (c) Time series of wind stress estimated from the European Centre for Medium-Range Weather Forecasting (ECMWF) reanalysis winds (black) and the K1 buoy measurements (gray). (d) Time series of near-inertial wind work computed from the ECMWF reanalysis winds and observed mixed-layer near-inertial currents (blue), and from the slab model driven by the ECMWF reanalysis winds (black). (e) Time integral of (d) showing the cumulative wind energy input to the mixed layer from each flux estimate for the central mooring deployment period. (f) Time series of Wentzel-Kramers-Brillouin (WKB)-scaled near-inertial kinetic energy observed by the current meters at the central mooring. The blue and pink lines, respectively, indicate the glider-based mixed layer depth H_{ML} and the H^* scaling (Section 3.1). Periods of the six near-inertial events are shaded gray in (c–e) and are labeled in (e). The duration of each event is mainly chosen to include near-inertial energy peaks from all moorings. The estimated downward group velocity of each event is indicated in (f).

The central and four inner moorings were also instrumented with 75-KHz unit upward-looking Acoustic Doppler Current Profilers (ADCP) at about 450 m, which measured horizontal velocity in 8-m bins and formed ensembles every 60 min. In addition, the mooring measurements were complemented by hydrographic observations acquired by two ocean gliders that navigated in a bow-tie pattern across the mooring array for the entire sampling period (Damerell et al., 2016; Thompson et al., 2016). The mixed layer depth, H_{ML}, is calculated from coincident glider data using a threshold value of potential density increase ($\triangle\rho = 0.03$ kg m^{-3}) from a near-surface value at 10 m (Damerell et al., 2016).

Mooring measurements captured the mixed layer during winter and early spring months, and the pycnocline plus part of the ocean interior throughout the year. Horizontal velocity, temperature, salinity, and pressure observations

were obtained by ACMs and CTDs, with sampling intervals of 10 and 5 min, respectively. For each mooring, we linearly interpolated measurements of horizontal velocity, temperature, and salinity onto surfaces of constant depth at 10-m intervals between depths of 50 and 520 m, and onto uniform 10-min intervals between 5 September 2012 and 5 September 2013. Subsequently, the 10-min horizontal velocities were averaged onto hourly intervals.

2.2. Wind Data

The buoy of the OSMOSIS moorings contained meteorological sensors. Unfortunately, the buoy sank shortly after deployment. Wind data are instead taken from the European Centre for Medium-Range Weather Forecasting (ECMWF) ERA-Interim reanalysis surface wind fields (Dee et al., 2011). Zonal and meridional reanalysis winds are obtained at the grid point closest to the central mooring site with a time interval of 3 hr for the record year. Wind measurements from the K1 buoy, 250 km away from the OSMOSIS mooring site (Figure 1a), are used to validate the reanalysis wind fields. The K1 buoy was sampled at hourly intervals from 5 September to 28 December 2012. Wind speed was converted to stress using a speed-dependent drag coefficient (Large & Pond, 1981). The reanalysis winds show a good agreement with the measured winds, with a correlation coefficient of 0.74 (Figure 1c).

2.3. Band Pass Filtering

Moored horizontal velocities are bandpass filtered around the near-inertial frequency, where the near-inertial band (denoted by the subscript "*NI*") is defined as $\{0.9, 1.1\}f$, with $f = 2\,\Omega\sin\phi$ as the inertial frequency, Ω as the Earth's angular velocity, and ϕ as the latitude. The inertial period is approximately 16 hr at the OSMOSIS site. The rotary frequency spectra of horizontal velocity show a prominent peak rising within the near-inertial band for clockwise motions but not for counter-clockwise motions, consistent with the expectation that near-inertial flows are strongly clockwise-polarized (Figure S1 in Supporting Information S1). We did not find a significant sensitivity of our results (Section 3) to the bandwidth of the near-inertial band. Near-inertial velocity is isolated by means of a fourth-order Butterworth filter applied in the time domain. Following bandpassing, near-inertial kinetic energy and vertical shear are respectively quantified as $KE_{NI} = \frac{1}{2}\rho_0|\boldsymbol{u}_{NI}|^2$ and $S_{NI} = |\partial\boldsymbol{u}_{NI}/\partial z|^2$, where $\boldsymbol{u} = (u, v)$ is the horizontal velocity, $\rho_0 = 1{,}025$ kg m^{-3} is the reference density and z is the vertical coordinate. As previous OSMOSIS studies have shown that the region underwent a seasonal cycle in the vertical stratification (e.g., Buckingham et al., 2016; Erickson et al., 2020), monthly moving averaged buoyancy frequency is used to obtain "Wentzel-Kramers-Brillouin (WKB)" scaled near-inertial kinetic energy KE_{NI}^{WKB} and vertical shear S_{NI}^{WKB}. To account for vertical wavenumber changes, a WKB-stretched depth is applied (see the Supporting Information S1 for methodology). Further, the near-inertial wind work is defined as $\Pi_{NI} = \boldsymbol{\tau}_{NI} \cdot \boldsymbol{u}_{NI}$, where $\boldsymbol{\tau}$ is the surface wind stress vector and $\boldsymbol{u}_{NI}$ the mixed-layer near-inertial currents obtained from the shallowest available ACMs record in the central mooring ($\sim$50 m, 57.1% of the time during the year within the mixed layer).

3. Results

3.1. Annual Cycle of Wind-Generated Near-Inertial Waves

Near-inertial wind work is highly variable throughout the entire year, with the wind energy flux into near-inertial motions dominated by several intermittent events with duration of several days (Figure 1d). The cumulative near-inertial wind work with time shows a distinct "staircase" structure during the periods of strong resonant forcing (Figure 1e), which coincides well with the elevated KE_{NI}^{WKB} in the upper ocean (e.g., late December and mid-January; Figure 1f). These results suggest that the observed near-inertial energy is likely locally generated by surface wind forcing. This is further supported by the agreement between the near-inertial wind work estimated from the observed velocity and reanalysis winds and that from the slab model solely forced by the reanalysis winds (see the Supporting Information S1 for methodology). The typical amplitude of KE_{NI}^{WKB} during near-inertial wave events is of order 10 J m^{-3}, corresponding to a horizontal velocity scale of $\sim$0.1 m s^{-1}. This value is comparable in magnitude with the global average near-inertial velocity (Chaigneau et al., 2008; Park et al., 2005). Further, most of the increase in cumulative near-inertial wind work is seen in winter (December-March; Figure 1e), implying a seasonal cycle of wind-generated NIWs. The vertical profiles of KE_{NI}^{WKB} in winter and summer also denote the seasonality of near-inertial energy, with the magnitude being much higher in winter at all measured depths (Figure S2 in Supporting Information S1).

Plueddemann and Farrar (2006) found that the slab model might overestimate the near-inertial wind work, and Alford (2020) further indicated that this overestimation likely occurs when the mixed layer depth H_{ML} is shallow compared to the scaling $H^* = u^*/\sqrt{N^* f}$, where $u^* = \sqrt{\tau/\rho_{air}}$ is the friction velocity of the imposed stress, ρ_{air} the density of air, and N^* the buoyancy frequency just below the mixed layer. In the $H_{ML} \lesssim H^*$ case, the slab model may not account for the mixing and momentum injected by the winds. We examined this possibility in our data and found that the glider-derived mixed layer depth is largely deeper than H^* throughout the year, with the only exception in summer when KE_{NI}^{WKB} is weak (June-August).

### 3.2. Downward and Equatorward Propagation of Near-Inertial Waves

Six major near-inertial wave events are identified throughout the year (see Figure 1e), based on large wind stress ($\gtrsim 0.5$ N m^{-2}), net near-inertial wind energy input and enhanced near-inertial kinetic energy. In the vertical, a dominance of downward propagation is confirmed by the rotary vertical wavenumber spectra of KE_{NI}^{WKB} and S_{NI}^{WKB} (Figure S3 in Supporting Information S1), evidenced by the dominant clockwise rotation of horizontal velocity and shear vectors with depth (Leaman & Sanford, 1975). Then, the vertical group speed can be estimated by identifying the near-inertial wave packets and the associated downward progression of kinetic energy maxima over time (Figure 1f). We obtain a mean vertical group speed c_{gz}^{obs} with one standard deviation of 61 ± 13 m day^{-1} for the six identified near-inertial events. Following Vic et al. (2021), we use mooring-based vertical group speed and vertical phase speed to constrain the vertical wavenumber m. For waves with frequencies close to f, the equation for m is $\left(c_{\phi z}^{obs}\right)^2 m^2 - c_{gz}^{obs} f m - f^2 = 0$, where $c_{\phi z}^{obs}$ is the vertical phase speed computed by connecting the constant-phase velocity points as a function of depth. For the six near-inertial wave events, the mean vertical wavelength, $2\pi/m$, is quantified as 652 ± 185 m.

The spatial arrangement of the mooring array also allows us to explore the meridional propagation of NIWs. Comparison of the time series of KE_{NI}^{WKB} obtained from various moorings shows that the near-inertial kinetic energy peaks in the south almost always lag behind those in the north, suggesting that NIWs may propagate predominantly from north to south (i.e., equatorward in the Northern Hemisphere; Figure 2a). This indication of equatorward propagation is further confirmed by two lines of evidence. First, near-inertial kinetic energy within the mooring array is highly coherent, with the magnitude-squared coherence of near-inertial velocities ~0.8 between inner moorings and ~0.6 between outer moorings, consistent with all moorings having captured the same near-inertial wave events. Second, unlagged near-inertial kinetic energy peaks are commonly observed a few inertial periods before the lagged peaks (e.g., events 1,2,4,5), with the former stemming from circular inertial oscillations in the mixed layer and the latter from propagating NIWs below the mixed layer. Then, we quantify the meridional group velocity using their meridional distance and respective travel time. The travel time is identified as the temporal lag for which the lagged correlation of depth-averaged near-inertial kinetic energy in the northern and southern outer moorings is maximum. This gives a mean meridional group speed c_{gh}^{obs} of $5,875 \pm 864$ m day^{-1}.

The frequency and horizontal scale of NIWs can be diagnosed by linking the observed group speed estimates to the dispersion relation of NIWs (see the Supporting Information S1 for methodology), which is written as $\left(\omega^2 - f^2\right) m^2 = N^2 k_h^2$, where ω is the frequency and k_h the horizontal wavenumber. The observed c_{gz}^{obs} and c_{gh}^{obs} are broadly consistent with the resulting dispersion curves in Figures 2b–c. Based on these wave properties, we can obtain the mean frequency $\omega = 1.039 \pm 0.018 f$ and the horizontal wavelength $2\pi/k_h = 79 \pm 28$ km from the dispersion relation. The latter is consistent with the frequency structure function diagnostics of Callies et al. (2020), who concluded that near-inertial motions have horizontal wavelengths larger than the largest scale sampled by the outer mooring array. Detailed properties of the six near-inertial events are given in Table S1 of Supporting Information S1.

3.3. Chimney Effect

To assess the inertial chimney effect at different spatial scales, the vertical component of the relative vorticity, $\zeta = \frac{\partial v}{\partial x} - \frac{\partial u}{\partial y}$, is respectively estimated from velocity gradients from the inner and outer mooring clusters. The chimney effect for near-inertial kinetic energy and vertical shear is illustrated by Figure 3, which displays
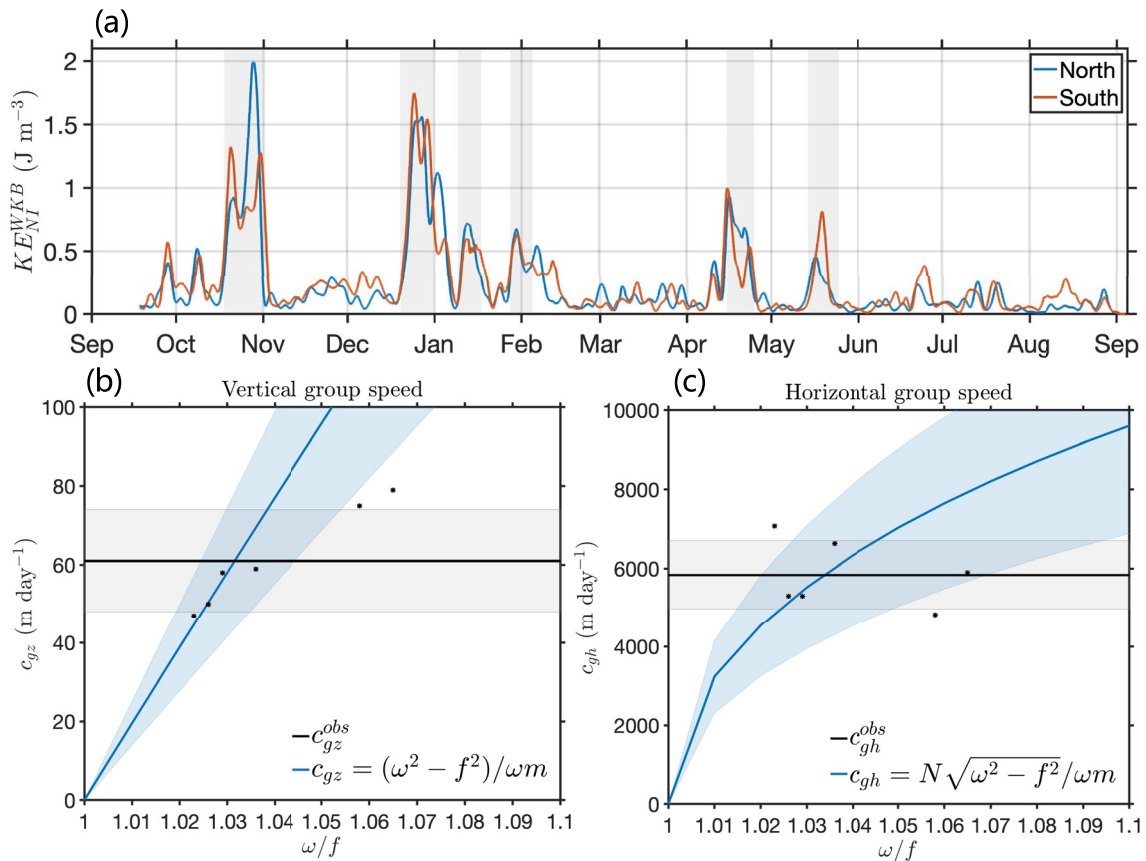
Figure 2. (a) Time series of Wentzel-Kramers-Brillouin (WKB)-scaled near-inertial kinetic energy estimated from outer moorings in the north (blue) and south (orange). Both estimates are low-pass filtered over 14.5 hr (corresponding to a frequency of $1.1f$) to remove tidal and higher-frequency signals, and are then depth-averaged over all observed depths (50–520 m). (b) Comparison of six event-averaged vertical group speed estimates from observations (black) and from the dispersion curve for $m = 2\pi/652$ m (blue). The shading represents one standard deviation. (c) Same as (b) but for horizontal group speed. Scattered dots in (b–c) represent estimates of the six near-inertial wave events.

the two-dimensional probability density functions of Rossby number, ζ/f, against KE_{NI}^{WKB} and S_{NI}^{WKB} and their associated vertical structures. All terms are computed at the central mooring site, and include all observed depths (50–520 m). For both spatial scales, near-inertial kinetic energy (Figures 3a and 3b) and vertical shear (Figures 3d and 3e) are found to be significantly intensified in regions of anticyclonic vorticity (i.e., $\zeta/f < 0$). Such intensification in anticyclonic regimes is more apparent for near-inertial kinetic energy, which is typically contained mostly in the first few vertical modes (e.g., Raja et al., 2022), compared to near-inertial vertical shear, which is contained mostly in higher vertical modes (e.g., Alford et al., 2017). Note that horizontal scales of O(1 km) and O(10 km) are expected to be resolved by the inner and outer mooring clusters, respectively. The inner mooring-based Rossby number ζ_{Inner}/f reflects the signature of submesoscale flows with a positive skewness (Buckingham et al., 2016) and a range from -0.8 to 1.2, which is 2–3 times larger than the outer mooring-based Rossby number ζ_{Outer}/f of -0.4 to 0.4 (cf. Figures 3a and 3b). However, the enhanced near-inertial kinetic energy and vertical shear are only focused in anticyclonic regions with Rossby number values of order 0.1, rather than with those of order 1. This suggests that mesoscale anticyclones play a predominant role in determining the chimney effect.

Submesoscale processes are embedded in the field of mesoscale motions in the inner-mooring diagnostics (Figures 3a and 3d). To isolate the submesoscale effect, we estimate the submesoscale vorticity anomaly relative to the mesoscale background, that is, $\zeta_{Inner} - \zeta_{Outer}$. Figures 3c and 3f show that the association of enhanced KE_{NI}^{WKB} and S_{NI}^{WKB} with $(\zeta_{Inner} - \zeta_{Outer})/f$ is greatly reduced, providing further evidence that the role played by submesoscale motions is modest and thus the observed chimney effect is attributed to mesoscale motions. Note, however, that submesoscale motions with spatial scales smaller than the inner mooring array are not resolved,
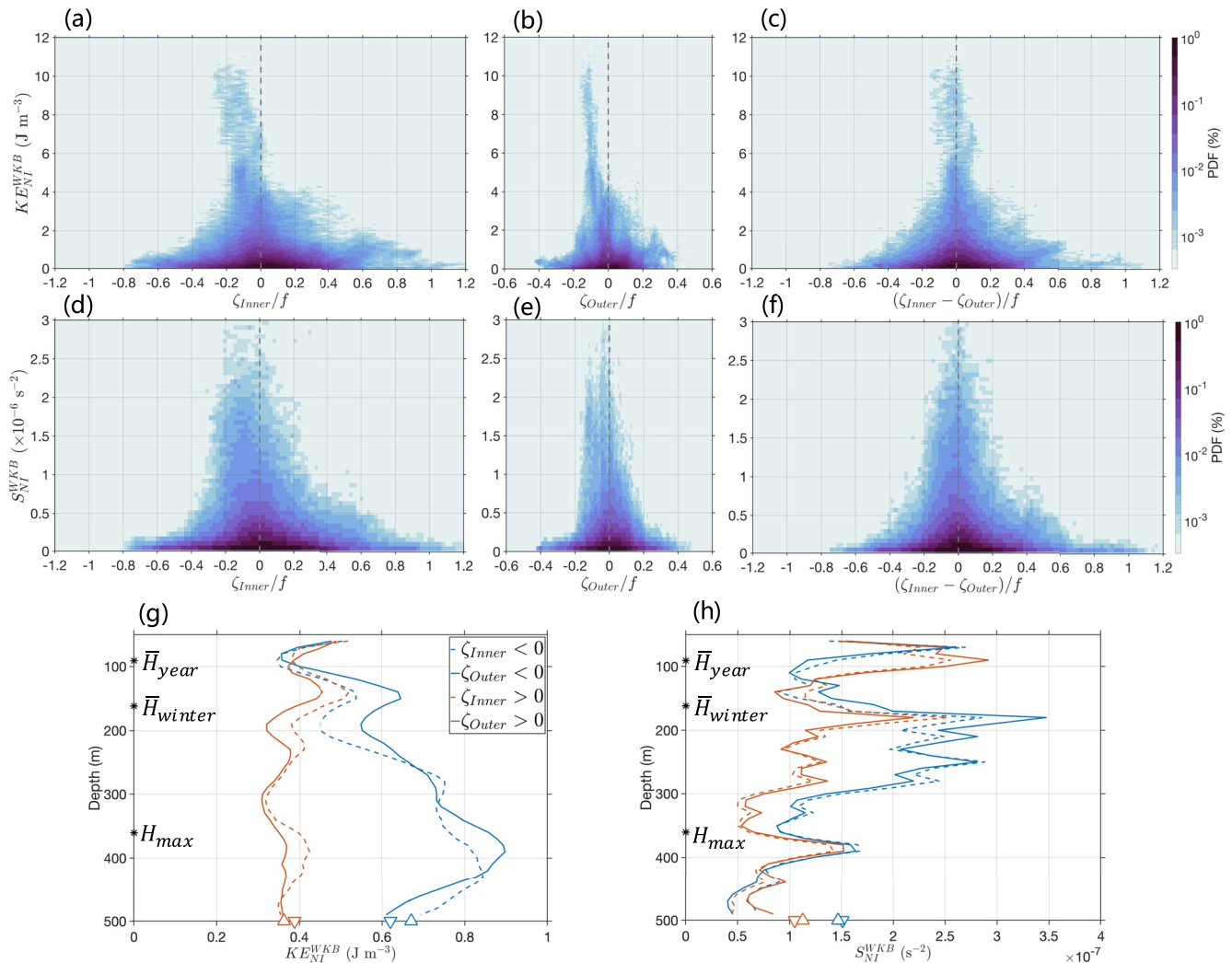
Figure 3. Two-dimensional probability density function of Wentzel-Kramers-Brillouin (WKB)-scaled near-inertial kinetic energy at the central mooring site, KE_{NI}^{WKB}, and Rossby number estimated from (a) the inner moorings, ζ_{Inner}/f, (b) the outer moorings, ζ_{Outer}/f, and (c) their difference, $(\zeta_{Inner} - \zeta_{Outer})/f$. (d–f) Same as (a–c) but for WKB-scaled near-inertial vertical shear, S_{NI}^{WKB}. Annual-averaged composite profiles of (g) KE_{NI}^{WKB} and (h) S_{NI}^{WKB} for positive and negative Rossby numbers. The annual-averaged, winter-averaged and maximum mixed layer depths, denoted by $\overline{H}_{year}$, $\overline{H}_{winter}$ and H_{max}, are marked on the y axis of (g–h). The upward-pointing and downward-pointing triangles on the x axis of (g–h) denote the averaged KE_{NI}^{WKB} and S_{NI}^{WKB} conditioned on the sign of vorticity from the outer and inner mooring clusters, respectively.

and their role in modulating the chimney effect cannot be assessed. The detailed evolution of a near-inertial wave event with a mesoscale anticyclonic environment is provided in Figures S4 and S5 in Supporting Information S1, which illustrate the sequence from the wind forcing of mixed-layer inertial currents into NIWs shown as a set of discrete downward and rightward swaths below the mixed layer after approximately eight inertial periods. During the downward-propagating period, the mooring site was located inside an anticyclonic eddy with a Rossby number of order −0.1, as estimated from both the outer moorings and altimetric measurements.

We next examine the vertical structures of KE_{NI}^{WKB} and S_{NI}^{WKB} in regions of negative and positive vorticity (Figures 3g and 3h). The annual-averaged mixed layer depth is about 90 m. In the mixed layer, both KE_{NI}^{WKB} and S_{NI}^{WKB} show no clear dependence on relative vorticity. The muted chimney effect in the mixed layer is expected because wind-forced near-inertial oscillations are purely horizontal and thus are not influenced by the sign of relative vorticity (also see Figure 4). Below the base of the mixed layer, however, KE_{NI}^{WKB} associated with anticyclonic vorticity is substantially more energetic than that associated with cyclonic vorticity, typically by a factor of 2–3. This illustrates that near-inertial kinetic energy preferentially progresses downward in the presence of anticyclonic structures. In particular, the magnitude of KE_{NI}^{WKB} associated with anticyclonic vorticity gradually
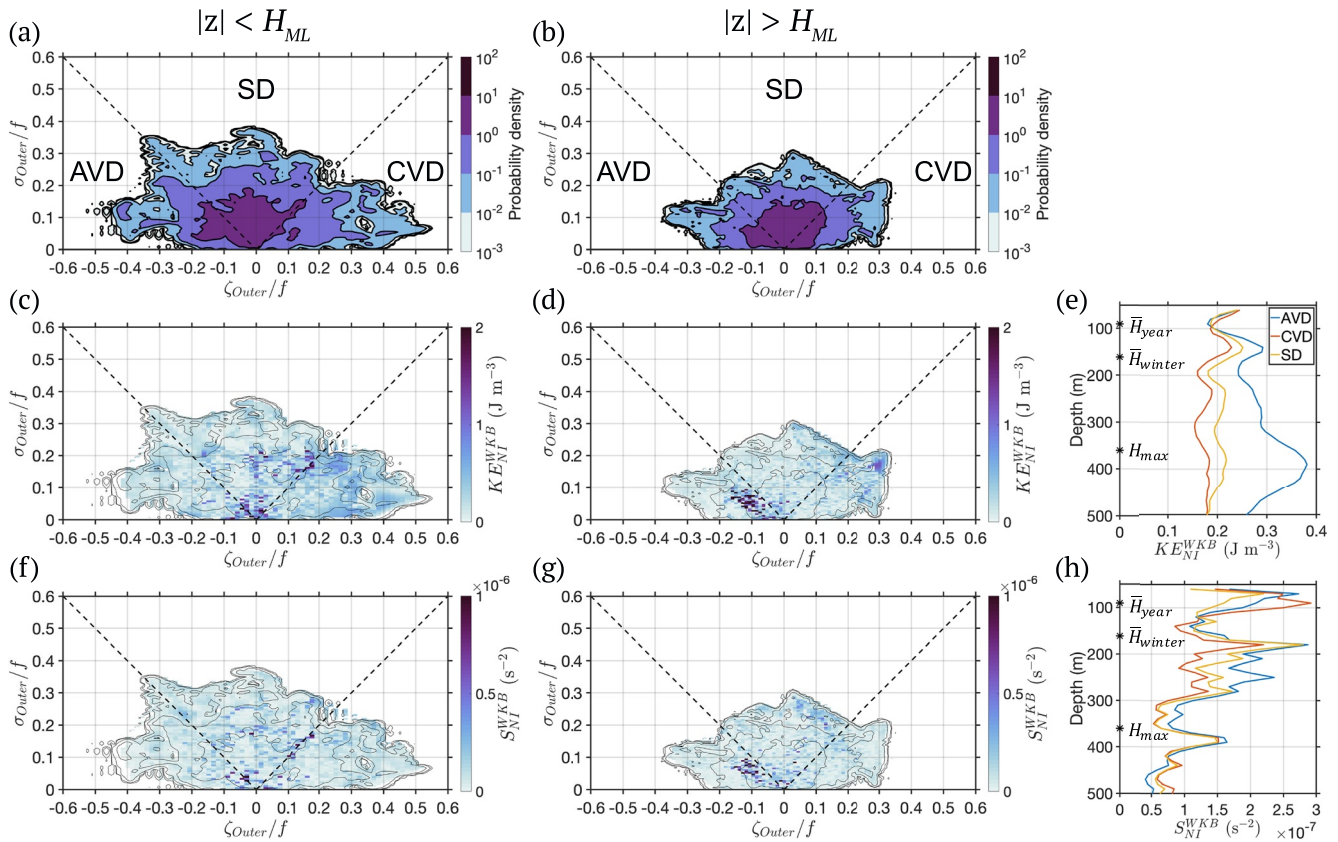
Figure 4. Vorticity-strain joint probability distribution function estimated from the outer moorings (a) within the mixed layer $|z| < H_{ML}$ and (b) below the mixed layer $|z| > H_{ML}$. The x-y space is divided into three regions: anticyclonic vorticity dominated (AVD), cyclonic vorticity dominated (CVD), and strain dominated (SD). Conditional mean of (c–d) KE_{NI}^{WKB} and (f–g) S_{NI}^{WKB} conditioned on the vorticity and strain in the two vertical parts, contoured by the respective probability density. Annual-averaged composite profiles of (e) KE_{NI}^{WKB} and (h) S_{NI}^{WKB} for the AVD, CVD and SD regions. The annual-averaged, winter-averaged, and maximum mixed layer depths, respectively denoted by $\overline{H}_{year}$, $\overline{H}_{winter}$ and H_{max}, are marked on the y axis of panels (e) and (h).

increases with depth and peaks at 400 m, consistent with an accumulation of trapped near-inertial kinetic energy at depth.

Compared to the cumulative behavior of KE_{NI}^{WKB} with depth, S_{NI}^{WKB} exhibits a different vertical structure. The peaks of S_{NI}^{WKB} associated with both cyclonic and anticyclonic vorticity are found around 180 m, which is very close to the mean mixed layer depth during winter (Figure 3h). Beneath 180 m, S_{NI}^{WKB} associated with cyclonic vorticity rapidly decreases from 2.5×10^{-7} s^{-2} to about 1×10^{-7} s^{-2}, and remains at this approximate magnitude down to 500 m. In contrast, S_{NI}^{WKB} associated with anticyclonic vorticity persists with an elevated magnitude of 2.5×10^{-7} s^{-2} until an abrupt decrease occurs at approximately 300 m. Notably, S_{NI}^{WKB} in anticyclonic regions is always larger than that in cyclonic regions from 180 m down to approximately the deepest mixed layer depth of 360 m. Below 360 m, S_{NI}^{WKB}, again, shows no dependence on vorticity and gently decays with depth. These results suggest that high-mode NIWs, which are expected to dominate vertical shear, are likely dissipated near the base of the mixed layer, and only low-mode NIWs propagate further downward. We acknowledge, however, that accurate quantification of near-inertial kinetic energy distribution in barotropic and baroclinic modes from the moorings is particularly challenging, due to the limited sampling range (approximately one-tenth of the full water column and one half of the water column above the mode-1 zero crossing; see Figure S6 in Supporting Information S1).

Apart from the background vorticity field, mesoscale straining processes may also affect the vertical propagation of NIWs (Asselin et al., 2020; Bühler & McIntyre, 2005; Noh & Nam, 2021). To further link the chimney effect to ambient flow properties, it can be instructive to apply the vorticity-strain parameter space (Balwada et al., 2021), which allows us to distinguish between strain-dominated regions (SD; i.e., fronts), anticyclonic vorticity-dominated regions (AVD; i.e., anticyclonic eddies) and cyclonic vorticity-dominated regions (CVD;

i.e., cyclonic eddies). We examine the distributions of KE_{NI}^{WKB} and S_{NI}^{WKB} conditioned on the joint probability distribution function of the outer mooring-based vorticity and strain within the mixed layer ($|z| < H_{ML}$) and below the mixed layer ($|z| > H_{ML}$) (Figures 4a and 4b). The strain rate is defined as $\sigma = \left[\left(\frac{\partial u}{\partial x} - \frac{\partial v}{\partial y} \right)^2 + \left(\frac{\partial u}{\partial y} - \frac{\partial v}{\partial x} \right)^2 \right]^{1/2}$. The joint probability distribution functions below and within the mixed layer are qualitatively symmetric regarding vorticity, as expected at the mesoscales (Vic et al., 2022). Within the mixed layer, KE_{NI}^{WKB} and S_{NI}^{WKB} are homogeneously distributed in vorticity-strain space (Figures 4c and 4e). However, below the mixed layer, the largest values of KE_{NI}^{WKB} and S_{NI}^{WKB} are found in the AVD region (Figures 4d and 4f). This preference is also seen in the vertical structures of KE_{NI}^{WKB} and S_{NI}^{WKB} in the regions of AVD, CVD, and SD (Figures 4g and 4h), in particular for KE_{NI}^{WKB}. While the straining processes may have played a role in the conversion from inertial oscillations to NIWs, the deep penetration of NIWs is found to be mostly in anticyclonic eddies rather than in the strained regions. A similar pattern has been found through analysis of the inner moorings (Figure S7 in Supporting Information S1). This confirms that mesoscale anticyclonic eddies are the primary factors facilitating the deep penetration of surface-generated NIWs. The little influence of strain on NIWs conforms to expectations from the wave escape mechanism (Rocha et al., 2018), and was also reported in a dipole vortex in the Iceland Basin (Thomas et al., 2020).

4. Summary and Discussion

In this work, we have examined the annual cycle of NIWs in a typical open-ocean region at midlatitudes based on mooring observations. Our main findings are summarized as follows: (a) Local wind forcing is the main factor in generating near-inertial motions in the OSMOSIS region. Near-inertial kinetic energy is dominated by intermittent wind events of a few days duration, and shows a seasonal cycle in energy level, elevated in winter and reduced in summer. (b) Wind-generated NIWs are found to predominately propagate equatorward and downward, with estimated horizontal group speeds two orders of magnitude larger than vertical group speeds. (c) The properties of NIWs have been estimated using the dispersion relation and observations, yielding an annual-mean frequency of $1.039f$, a vertical wavelength of 652 m and a horizontal wavelength of 79 km. We also demonstrate that the meridional group speed can be predicted from the vertical group speed diagnosed from a single mooring combined with the dispersion relation. (d) The penetration of near-inertial kinetic energy and vertical shear into the ocean interior is facilitated by mesoscale anticyclonic eddies with Rossby number of O(0.1) rather than submesoscale anticyclonic eddies with Rossby number of O(1).

Our results add observational evidence for equatorward propagation of locally wind-generated NIWs, which conforms to expectations from the free propagation of NIWs due to β-refraction (Garrett, 2001). That is, waves generated at f, the local lowest internal wave frequency, must propagate equatorward into a latitude with an inertial frequency lower than f. The energy flux of these equatorward-propagating NIWs is dominated by low modes (Alford, 2003), which are associated with a faster group velocity compared to high modes and are typically expected to propagate over long distances.

The vertical structures of the chimney effect in mesoscale and submesoscale anticyclones do not show a distinct difference (Figures 3g and 3h), suggesting that submesoscale processes may not substantially modify the penetration of NIWs. There are three reasons for the modest effect from the submesoscale. First, submesoscale motions are typically confined to the mixed layer of O(100 m) and weaken in the ocean interior. Mixed-layer inertial oscillations may undergo lateral de-phasing caused by submesoscale motions, which would produce downward-propagating NIWs with small vertical scales, and thus the resulting vertical group velocity would be small. By contrast, mesoscale eddies are featured with a much larger vertical scale on the order of 1,000 m, and thus can be a primary player in setting the inertial chimney effect at depth. Second, the spatial scale of submesoscales is comparable to the local mixed-layer Rossby radius of 1–4 km (Callies et al., 2020; Yu et al., 2019), which is considerably smaller than the diagnosed spatial scale of NIWs ($2\pi/k_h = 79$ km). Third, both NIWs and submesoscale fronts are intermittent and short-lived in the study region, and thus the concurrence of both processes is even rarer.

Lastly, this study points out the importance of the inertial chimney effect in determining surface-generated near-inertial kinetic energy propagation into the ocean interior. However, the interactions of NIWs with eddies and associated energy transfers are not a direct consequence of the chimney effect. It has recently been suggested

that the presence of NIWs can result in a substantial reduction of mesoscale kinetic energy by stimulating a forward energy cascade at partially balanced submesoscale fronts (Barkan et al., 2021). The assessment and quantification of such cross-scale energy transfers using the OSMOSIS observations are under way.

Data Availability Statement

All OSMOSIS mooring and glider data are freely available, and are archived at the British Oceanographic Data Centre. Moored observations can be obtained from https://www.bodc.ac.uk/projects/data_management/uk/osmosis/, and glider data are accessible at https://doi.org/10.5285/6cf0b33e-a192-549f-e053-6c86abc01204. ERA-Interim data were obtained from the European Centre for Medium-Range Weather Forecasts (downloaded from http://www.ecmwf.int/en/research/climate-reanalysis/era-interim).

References

Alford, M. H. (2003). Redistribution of energy available for ocean mixing by long-range propagation of internal waves. *Nature*, *423*(6936), 159–162. https://doi.org/10.1038/nature01628

Alford, M. H. (2020). Revisiting near-inertial wind work: Slab models, relative stress, and mixed layer deepening. *Journal of Physical Oceanography*, *50*(11), 3141–3156. https://doi.org/10.1175/jpo-d-20-0105.1

Alford, M. H., MacKinnon, J. A., Pinkel, R., & Klymak, J. M. (2017). Space–time scales of shear in the North Pacific. *Journal of Physical Oceanography*, *47*(10), 2455–2478. https://doi.org/10.1175/jpo-d-17-0087.1

Alford, M. H., MacKinnon, J. A., Simmons, H. L., & Nash, J. D. (2016). Near-inertial internal gravity waves in the ocean. *Annual Review of Marine Science*, *8*(1), 95–123. https://doi.org/10.1146/annurev-marine-010814-015746

Alford, M. H., & Zhao, Z. X. (2007). Global patterns of low-mode internal-wave propagation. part i: Energy and energy flux. *Journal of Physical Oceanography*, *37*(7), 1829–1848. https://doi.org/10.1175/jpo3085.1

Asselin, O., Thomas, L. N., Young, W. R., & Rainville, L. (2020). Refraction and straining of near-inertial waves by barotropic eddies. *Journal of Physical Oceanography*, *50*(12), 3439–3454. https://doi.org/10.1175/jpo-d-20-0109.1

Asselin, O., & Young, W. R. (2020). Penetration of wind-generated near-inertial waves into a turbulent ocean. *Journal of Physical Oceanography*, *50*(6), 1699–1716. https://doi.org/10.1175/jpo-d-19-0319.1

Balwada, D., Xiao, Q., Smith, S., Abernathey, R., & Gray, A. R. (2021). Vertical fluxes conditioned on vorticity and strain reveal submesoscale ventilation. *Journal of Physical Oceanography*, *51*(9), 2883–2901. https://doi.org/10.1175/jpo-d-21-0016.1

Barkan, R., Srinivasan, K., Yang, L., McWilliams, J. C., Gula, J., & Vic, C. (2021). Oceanic mesoscale eddy depletion catalyzed by internal waves. *Geophysical Research Letters*, *48*(18), e2021GL094376. https://doi.org/10.1029/2021gl09437

Buckingham, C. E., Garabato, A. C. N., Thompson, A. F., Brannigan, L., Lazar, A., Marshall, D. P., et al. (2016). Seasonality of submesoscale flows in the ocean surface boundary layer. *Geophysical Research Letters*, *43*(5), 2118–2126. https://doi.org/10.1002/2016gl068009

Buckingham, C. E., Lucas, N. S., Belcher, S. E., Rippeth, T. P., Grant, A. L. M., Le Sommer, J., et al. (2019). The contribution of surface and submesoscale processes to turbulence in the open ocean surface boundary layer. *Journal of Advances in Modeling Earth Systems*, *11*(12), 4066–4094. https://doi.org/10.1029/2019ms001801

Bühler, O., & McIntyre, M. E. (2005). Wave capture and wave–vortex duality. *Journal of Fluid Mechanics*, *534*, 67–95. https://doi.org/10.1017/s0022112005004374

Callies, J., Barkan, R., & Naveira Garabato, A. C. (2020). Time scales of submesoscale flow inferred from a mooring array. *Journal of Physical Oceanography*, *50*(4), 1065–1086. https://doi.org/10.1175/jpo-d-19-0254.1

Chaigneau, A., Pizarro, O., & Rojas, W. (2008). Global climatology of near-inertial current characteristics from Lagrangian observations. *Geophysical Research Letters*, *35*(13), L13603. https://doi.org/10.1029/2008gl034060

Damerell, G. M., Heywood, K. J., Thompson, A. F., Binetti, U., & Kaiser, J. (2016). The vertical structure of upper ocean variability at the porcupine abyssal plain during 2012-2013. *Journal of Geophysical Research: Oceans*, *121*(5), 3075–3089. https://doi.org/10.1002/2015jc011423

Dee, D. P., Uppala, S. M., Simmons, A. J., Berrisford, P., Poli, P., Kobayashi, S., et al. (2011). The era-interim reanalysis: Configuration and performance of the data assimilation system. *Quarterly Journal of the Royal Meteorological Society*, *137*(656), 553–597. https://doi.org/10.1002/qj.828

Egbert, G. D., & Ray, R. D. (2000). Significant dissipation of tidal energy in the deep ocean inferred from satellite altimeter data. *Nature*, *405*(6788), 775–778. https://doi.org/10.1038/35015531

Erickson, Z. K., Thompson, A. F., Callies, J., Yu, X. L., Garabato, A. N., & Klein, P. (2020). The vertical structure of open-ocean submesoscale variability during a full seasonal cycle. *Journal of Physical Oceanography*, *50*(1), 145–160. https://doi.org/10.1175/jpo-d-19-0030.1

Ferrari, R., & Wunsch, C. (2009). Ocean circulation kinetic energy: Reservoirs, sources, and sinks. *Annual Review of Fluid Mechanics*, *41*(1), 253–282. https://doi.org/10.1146/annurev.fluid.40.111406.102139

Fu, L. L. (1981). Observations and models of inertial waves in the deep ocean. *Reviews of Geophysics*, *19*(1), 141–170. https://doi.org/10.1029/rg019i001p00141

Garrett, C. (2001). What is the "near-inertial" band and why is it different from the rest of the internal wave spectrum? *Journal of Physical Oceanography*, *31*(4), 962–971. https://doi.org/10.1175/1520-0485(2001)031<0962:witnib>2.0.co;2

Gill, A. E. (1984). On the behavior of internal waves in the wakes of storms. *Journal of Physical Oceanography*, *14*(7), 1129–1151. https://doi.org/10.1175/1520-0485(1984)014<1129:otboiw>2.0.co;2

Huang, R., Xie, X., Hu, J., & Sun, Z. (2021). Poleward propagation of typhoon-induced near-inertial waves in the northern south China sea. *Frontiers in Marine Science*, *8*, 713991. https://doi.org/10.3389/fmars.2021.713991

Jeon, C., Park, J.-H., Nakamura, H., Nishina, A., Zhu, X.-H., Kim, D. G., et al. (2019). Poleward-propagating near-inertial waves enabled by the Western boundary current. *Scientific Reports*, *9*(1), 9955. https://doi.org/10.1038/s41598-019-46364-9

Jiang, J., Lu, Y. Y., & Perrie, W. (2005). Estimating the energy flux from the wind to ocean inertial motions: The sensitivity to surface wind fields. *Geophysical Research Letters*, *32*(15), L15610. https://doi.org/10.1029/2005gl023289

Kunze, E. (1985). Near-inertial wave-propagation in geostrophic shear. *Journal of Physical Oceanography*, *15*(5), 544–565. https://doi.org/10.1175/1520-0485(1985)015<0544:niwpig>2.0.co;2

Large, W. G., & Pond, S. (1981). Open ocean momentum flux measurements in moderate to strong winds. *Journal of Physical Oceanography*, *11*(3), 324–336. https://doi.org/10.1175/1520-0485(1981)011<0324:oomfmi>2.0.co;2

Leaman, K. D., & Sanford, T. B. (1975). Vertical energy propagation of inertial waves - Vector spectral analysis of velocity profiles. *Journal of Geophysical Research*, *80*(15), 1975–1978. https://doi.org/10.1029/jc080i015p01975

Lee, D.-K., & Niiler, P. P. (1998). The inertial chimney: The near-inertial energy drainage from the ocean surface to the deep layer. *Journal of Geophysical Research*, *103*(C4), 7579–7591. https://doi.org/10.1029/97jc03200

Naveira Garabato, A. C., Yu, X., Callies, J., Barkan, R., Polzin, K. L., Frajka-Williams, E., et al. (2022). Kinetic energy transfers between mesoscale and submesoscale motions in the open ocean's upper layers. *Journal of Physical Oceanography*, *52*(1), 75–97. https://doi.org/10.1175/jpo-d-21-0099.1

Noh, S., & Nam, S. (2021). Nonseasonal variations in near-inertial kinetic energy observed far below the surface mixed layer in the southwestern east sea (Japan Sea). *Journal of Marine Science and Engineering*, *10*(1), 9. https://doi.org/10.3390/jmse10010009

Park, J. J., Kim, K., & King, B. A. (2005). Global statistics of inertial motions. *Geophysical Research Letters*, *32*(14), L14612. https://doi.org/10.1029/2005gl023258

Plueddemann, A. J., & Farrar, J. T. (2006). Observations and models of the energy flux from the wind to mixed-layer inertial currents. *Deep Sea Research Part II: Topical Studies in Oceanography*, *53*(1–2), 5–30. https://doi.org/10.1016/j.dsr2.2005.10.017

Qu, L., Thomas, L., & Gula, J. (2021). Bottom mixing enhanced by tropical storm-generated near-inertial waves entering critical layers in the Straits of Florida. *Geophysical Research Letters*, *48*(15), e2021GL093773. https://doi.org/10.1029/2021gl093773

Raja, K. J., Buijsman, M. C., Shriver, J. F., Arbic, B. K., & Siyanbola, O. (2022). Near-inertial wave energetics modulated by background flows in a global model simulation. *Journal of Physical Oceanography*, *52*(5), 823–840. in press. https://doi.org/10.1175/JPO-D-21-0130.1

Rimac, A., von Storch, J. S., Eden, C., & Haak, H. (2013). The influence of high-resolution wind stress field on the power input to near-inertial motions in the ocean. *Geophysical Research Letters*, *40*(18), 4882–4886. https://doi.org/10.1002/grl.50929

Rocha, C. B., Wagner, G. L., & Young, W. R. (2018). Stimulated generation: Extraction of energy from balanced flow by near-inertial waves. *Journal of Fluid Mechanics*, *847*, 417–451. https://doi.org/10.1017/jfm.2018.308

Schlosser, T. L., Jones, N. L., Bluteau, C. E., Alford, M. H., Ivey, G. N., & Lucas, A. J. (2019). Generation and propagation of near-inertial waves in a baroclinic current on the Tasmanian Shelf. *Journal of Physical Oceanography*, *49*(10), 2653–2667. https://doi.org/10.1175/jpo-d-18-0208.1

Silverthorne, K. E., & Toole, J. M. (2009). Seasonal kinetic energy variability of near-inertial motions. *Journal of Physical Oceanography*, *39*(4), 1035–1049. https://doi.org/10.1175/2008jpo3920.1

Simmons, H. L., & Alford, M. H. (2012). Simulating the long-range swell of internal waves generated by ocean storms. *Oceanography*, *25*(2), 30–41. https://doi.org/10.5670/oceanog.2012.39

Thomas, L. N., Rainville, L., Asselin, O., Young, W. R., Girton, J., Whalen, C. B., et al. (2020). Direct observations of near-inertial wave ζ-refraction in a dipole vortex. *Geophysical Research Letters*, *47*(21), e2020GL090375. https://doi.org/10.1029/2020gl090375

Thomas, L. N., & Zhai, X. (2022). Chapter 5 - The lifecycle of surface-generated near-inertial waves. In M. Meredith & A. Naveira Garabato (Eds.), *ocean mixing* (pp. 95–115). Elsevier.

Thompson, A. F., Lazar, A., Buckingham, C., Garabato, A. C. N., Damerell, G. M., & Heywood, K. J. (2016). Open-ocean submesoscale motions: A full seasonal cycle of mixed layer instabilities from gliders. *Journal of Physical Oceanography*, *46*(4), 1285–1307. https://doi.org/10.1175/jpo-d-15-0170.1

Tort, M., & Winters, K. B. (2018). Poleward propagation of near-inertial waves induced by fluctuating winds over a baroclinically unstable zonal jet. *Journal of Fluid Mechanics*, *834*, 510–530. https://doi.org/10.1017/jfm.2017.698

Vic, C., Ferron, B., Thierry, V., Mercier, H., & Lherminier, P. (2021). Tidal and near-inertial internal waves over the Reykjanes Ridge. *Journal of Physical Oceanography*, *51*(2), 419–437. https://doi.org/10.1175/jpo-d-20-0097.1

Vic, C., Hascoët, S., Gula, J., Huck, T., & Maes, C. (2022). Oceanic mesoscale cyclones cluster surface Lagrangian material. *Geophysical Research Letters*, *49*(4), e2021GL097488. https://doi.org/10.1029/2021gl097488

Whalen, C. B., de Lavergne, C., Naveira Garabato, A. C., Klymak, J. M., MacKinnon, J. A., & Sheen, K. L. (2020). Internal wave-driven mixing: Governing processes and consequences for climate. *Nature Reviews Earth & Environment*, *1*(11), 606–621. https://doi.org/10.1038/s43017-020-0097-z

Yu, X., Naveira Garabato, A. C., Martin, A. P., Buckingham, C. E., Brannigan, L., & Su, Z. (2019). An annual cycle of submesoscale vertical flow and restratification in the upper ocean. *Journal of Physical Oceanography*, *49*(6), 1439–1461. https://doi.org/10.1175/jpo-d-18-0253.1

Yu, X., Naveira Garabato, A. C., Martin, A. P., & Marshall, D. P. (2021). The annual cycle of upper-ocean potential vorticity and its relationship to submesoscale instabilities. *Journal of Physical Oceanography*, *51*(2), 385–402. https://doi.org/10.1175/jpo-d-20-0099.1

Zhai, X. M., Greatbatch, R. J., & Eden, C. (2007). Spreading of near-inertial energy in a 1/12°model of the north Atlantic Ocean. *Geophysical Research Letters*, *34*(10), L10609. https://doi.org/10.1029/2007gl029895

Zhai, X. M., Greatbatch, R. J., Eden, C., & Hibiya, T. (2009). On the loss of wind-induced near-inertial energy to turbulent mixing in the upper ocean. *Journal of Physical Oceanography*, *39*(11), 3040–3045. https://doi.org/10.1175/2009jpo4259.1

Zhai, X. M., Greatbatch, R. J., & Zhao, J. (2005). Enhanced vertical propagation of storm-induced near-inertial energy in an eddying ocean channel model. *Geophysical Research Letters*, *32*(18), L18602. https://doi.org/10.1029/2005gl023643

References From the Supporting Information

Alford, M. H., Cronin, M. F., & Klymak, J. M. (2012). Annual cycle and depth penetration of wind-generated near-inertial internal waves at ocean station papa in the northeast Pacific. *Journal of Physical Oceanography*, *42*(6), 889–909. https://doi.org/10.1175/jpo-d-11-092.1

Bell, T. H. (1974). Processing vertical internal wave spectra. *Journal of Physical Oceanography*, *4*, 669–670. https://doi.org/10.1175/1520-0485(1974)004<0669:pviws>2.0.co;2

D'Asaro, E. A. (1985). The energy flux from the wind to near-inertial motions in the surface mixed layer. *Journal of Physical Oceanography*, *15*(8), 1043–1059. https://doi.org/10.1175/1520-0485(1985)015<1043:tefftw>2.0.co;2

Duda, T. F., & Cox, C. S. (1989). Vertical wave number spectra of velocity and shear at small internal wave scales. *Journal of Geophysical Research*, *94*(C1), 939. https://doi.org/10.1029/jc094ic01p00939

Garcia, H. E., Boyer, T. P., Baranova, O. K., Locarnini, R. A., Mishonov, A. V., Grodsky, A., et al. (2019). In A. Mishonov (Ed.), *World ocean atlas 2018: Product documentation*.

Gill, A. E. (1982). *Atmosphere-ocean dynamics*. Academic Press.

Pollard, R. T., & Millard, R. C. (1970). Comparison between observed and simulated wind-generated inertial oscillations. *Deep-Sea Research*, *17*(4), 813–821. https://doi.org/10.1016/0011-7471(70)90043-4